A CT-based Monte Carlo simulation tool for dosimetry planning and analysis

J. J. DeMarco,[a)] T. D. Solberg, and J. B. Smathers

Jonsson Comprehensive Cancer Center, Department of Radiation Oncology, University of California Los Angeles, Los Angeles, California 90024-6951

The Los Alamos code MCNP4A (Monte Carlo N-Particle version 4A) is currently used to simulate a variety of problems ranging from nuclear reactor analysis to boron neutron capture therapy. A graphical user interface has been developed that automatically sets up the MCNP4A geometry and radiation source requirements for a three-dimensional Monte Carlo simulation using computed tomography data. The major drawback for this dosimetry system is the amount of time to obtain a statistically significant answer. A specialized patch file has been developed that optimizes photon particle transport and dose scoring within the standard MCNP4A lattice geometry. The transport modifications produce a performance increase (number of histories per minute) of approximately 4.7 based upon a 6 MV point source centered within a $30 \times 30 \times 30$ cm^3 lattice water phantom and $1 \times 1 \times 1$ mm^3 voxels. The dose scoring modifications produce a performance increase of approximately 470 based upon a tally section of greater than 1×10^4 lattice elements and a voxel size of 5 mm^3. Homogeneous and heterogeneous benchmark calculations produce good agreement with measurements using a standard water phantom and a high- and low-density heterogeneity phantom. The dose distribution from a typical mediastinum treatment planning setup is presented for qualitative analysis and comparison versus a conventional treatment planning system. © *1998 American Association of Physicists in Medicine.* [S0094-2405(98)00801-3]

Key words: Monte Carlo, treatment planning, computed tomography, dosimetry, inhomogeneity

I. INTRODUCTION

Radiotherapy treatment planning has evolved considerably in the last 25 yr with advances in computer hardware, image display, and plan evaluation tools. The calculation algorithms embedded in these systems are slowly changing, with a shift from correction-based methods to model-based methods such as a convolution calculation or the Monte Carlo method.[1,2] The Photon Treatment Planning Collaborative Working Group produced a comprehensive document evaluating the role of three-dimensional treatment planning in the treatment protocols for eight different anatomical sites.[3] The study evaluated various aspects related to three-dimensional treatment planning including calculation algorithms, dose-volume histograms, uncertainty analysis, numerical scoring of treatment plans, and inhomogeneity corrections. The general conclusion states that a three-dimensional (3-D) treatment planning system can significantly improve the planning process, allowing the clinician to evaluate the dose distribution based upon volumetric analysis using dose volume histograms and biological end points such as tumor control probability (TCP) and normal tissue complication probability (NTCP). The analysis of inhomogeneity corrections revealed many deficiencies regarding current CT-based correction methods. Using the one-dimensional effective pathlength (EPL) method, the group showed significant differences in the corrected plans for lung tumors and smaller differences for the other treatment sites. The final results are still in question due to the inability of the EPL correction to account for the transport of secondary electrons produced from a primary or secondary photon collision. The effects of bone heterogeneities such as the femoral heads is also in question since no heterogeneity correction accounts for the dose perturbation due to differences in atomic number. These types of studies emphasize the need for a dosimetry analysis tool that accounts for all aspects of primary and secondary particle transport within a patient-specific calculation geometry. With respect to the current dosimetry algorithms for radiotherapy planning, only the Monte Carlo method is currently able to account for all aspects of photon and electron transport within a heterogeneous medium.

In the area of radiotherapy treatment planning, Monte Carlo techniques represent a powerful tool for studying difficult radiation transport problems such as the effect of tissue heterogeneities and the separation of primary and scatter dose components. The major drawback for this type of approach has always been the amount of time necessary to produce a statistically meaningful result. With recent improvements in computer performance, however, the idea of routine treatment planning using Monte Carlo dose calculations has moved much closer to reality. The UCLA Department of Radiation Oncology is one of several institutions throughout the United States and the world that are actively developing Monte Carlo-based dosimetry systems including the OMEGA (Ottawa Madison Electron-Gamma Arrange) project at the University of Wisconsin,[4,5] the PEREGRINE. All Particle project at Lawrence Livermore National Laboratory,[6–8] the SBNCT (SUNY Boron Neutron Capture Therapy) project at University Hospital SUNY,[9] and NCT-

TABLE I. Element breakdown and density range for the five primary tissue types used with the CT-based geometry simulation. The weight percent for each element is taken from ICRU44.

	Lung	Fat	Water	Muscle	Bone
CT# range	$-930 \Leftrightarrow -200$	$-200 \Leftrightarrow -5$	$-5 \Leftrightarrow +5$	$+5 \Leftrightarrow +280$	$+280 \Leftrightarrow +1000$
ρ range	0.05–0.65	0.85–0.98	1.00	1.06–1.26	1.48–2.10
H ($Z=1$)	10.3	11.4	11.1	10.2	3.4
C ($Z=6$)	10.5	59.8	⋯	14.3	15.5
N ($Z=7$)	3.1	0.7	⋯	3.4	4.2
O ($Z=8$)	74.9	27.8	88.9	71.0	43.5
Na ($Z=11$)	0.2	0.1	⋯	0.1	0.1
Mg ($Z=12$)	⋯	⋯	⋯	⋯	0.2
P ($Z=15$)	0.2	⋯	⋯	0.2	10.3
S ($Z=16$)	0.3	0.1	⋯	0.3	0.3
Cl ($Z=17$)	0.3	0.1	⋯	0.1	⋯
K ($Z=19$)	0.2	⋯	⋯	0.4	⋯
Ca ($Z=20$)	⋯	⋯	⋯	⋯	22.5

PLAN at Tufts University and New England Medical Center Hospitals.[10]

The purpose of this study is the development of a photon and electron based dosimetry tool using the Los Alamos code MCNP4A (Monte Carlo N-Particle, version 4A). MCNP4A is a generalized Monte Carlo code capable of simulating coupled neutron–photon–electron problems using a three-dimensional, heterogeneous geometry system.[11,12] The boron neutron capture groups (SBNCT,NCTPLAN) use MCNP as the dose calculation engine for their treatment planning systems and have thus far developed their systems using the MCNP lattice geometry with a relatively coarse simulation voxel size of 1 cm^3. The scope of this paper will concentrate on three primary areas; manipulation of the generalized features of the code for CT-based photon and electron dosimetry applications, MCNP4A input modifications and algorithm development, and radiotherapy dosimetry examples.

II. MATERIALS AND METHODS

A. The Monte Carlo code system

MCNP4A will run on a variety of hardware platforms and supports a wide variety of tally/scoring features and variance reduction schemes. The photon physics treatment includes incoherent and coherent scattering, photoelectric absorption (with fluorescent emission) and pair production. The electron transport physics are based upon the Integrated Tiger Series (ITSv1.0) of codes,[13] a series of Monte Carlo transport codes (TIGER, CYLTRAN, and ACCEPT) that originated from the ET-RAN (Electron TRANsport) code[14] developed by Berger and Seltzer at the National Bureau of Standards for coupled electron–photon transport calculations. Rogers and Bielajew[15] have previously analyzed the energy-loss straggling formalism of earlier versions of ETRAN upon which ITSv1.0 is based. They show that the ETRAN/CYLTRAN treatment of collisional energy loss underestimates the energy loss in thin slabs of water by up to 10% between electron energies of 1–50 MeV. The Monte Carlo transport methods group at Los Alamos has successfully upgraded the MCNP electron physics algorithms to ITS version 3.0. ITSv3.0 implements several corrections for correctly sampling elec-

tron energy-loss straggling using the Landau distribution.[16,17] We are currently simulating all coupled photon–electron problems using a modified version of MCNP4A, which incorporates the electron transport modifications.

The conventional MCNP4A geometry package consists of first and second degree surfaces and fourth degree elliptical tori. On the basis of the simulation geometry, the user defines all surfaces and then combines the surfaces via Boolean operators to form cells. Attributes such as importance weighting, energy cutoff, and material define each cell. In addition to the conventional geometry package MCNP4A supports a nested lattice feature. The user defines one bounding cell, one lattice element (hexahedral or hexagonal), and the origin of the bounding cell. The code will automatically fill the bounding cell with the lattice element starting from the origin, creating a 3-D matrix of voxel elements.

B. Applications and the RTMCNP preprocessor

The MCNP4A Monte Carlo code requires a user defined input file containing the applicable geometry, source, and tally parameters. We are currently developing RTMCNP (Radiation Therapy MCNP), a preprocessor that provides a friendly interface between the user and the MCNP4A command structure. The lattice geometry will accept heterogeneous material data by filling the lattice with different material designations. RTMCNP automatically converts raw CT data from the UCLA Picture Archiving and Communication System (PACS) network into a manageable number of material designations. The CT data is binned into six major material groups; air, lung, fat, water, muscle, and bone. The approximate CT tissue ranges are taken from the data of Alfidi et al.[18] and verified using a GE9800 CT scanner. The elemental composition for lung, fat, muscle, and bone was obtained from ICRP23[19] and ICRU44[20] and is listed in Table I. The six primary groups are further subdivided with respect to density for a total of 17 material designations. The density variations are based upon the CT scanner calibration curve (electron density versus Hounsfield number) and the linear relationship between mass density and electron density.[21,22] RTMCNP currently supports all geometric parameters for

simulating the bremsstrahlung and electron contamination spectrum from the Philips SL-15 and SL-25 linear accelerators. The preprocessor utilizes this information to simulate multiple planar and noncoplanar beams incident on homogeneous and heterogeneous lattice phantoms as well as postprocessing of the tally information.

III. MCNP4A CODE MODIFICATIONS AND ALGORITHM DEVELOPMENT

A. Timing analysis

A timing analysis was performed on the code in order to determine the computationally expensive algorithms for a coupled photon–electron simulation. Three primary algorithms account for the run time of a simulation; photon transport, secondary electron transport, and the tally scheme for scoring energy deposition. The simulation is based upon a 6 MV isotropic point source at the center of a $30 \times 30 \times 30$ cm^3 water phantom. A voxel size of $5 \times 5 \times 5$ mm^3 (2.16×10^5 lattice elements) results in a run rate of 1778 source particles per minute for one SUN SPARC2 processor. A voxel size of $1 \times 1 \times 1$ mm^3 (2.7×10^7 lattice elements) corresponds to a run rate of 426 source particles per minute, approximately 4.2 times slower than the $5 \times 5 \times 5$ mm^3 example. The simulation performance is based upon the number of photons per minute, starting from the point source. MCNP4A allows the user to alter a variety of the fundamental photon and electron physics parameters in order to analyze primary particle transport and secondary particle production. In order to compare particle tracking performance with respect to primary photons and secondary particle production (photons and electrons), the biasing parameters BNUM, XNUM, RNOK, and ENUM were analyzed. These variables control the production of bremsstrahlung photons, electron induced x rays, knock-on electrons, and photon-induced secondary electrons, respectively. The default value for each parameter is unity in order to maintain an analog simulation. As the parameter is increased greater than one, the particle production is increased by that factor with an appropriate weight adjustment. The opposite is true when the parameter is decreased below unity. For a photon-based radiotherapy simulation, the biasing parameter ENUM represents the master variable since it controls the production of photon-induced secondary electrons and therefore the production of bremsstrahlung photons, electron-induced x rays, and knock-on electrons. The overhead associated with secondary electron production and transport versus primary photon transport can be analyzed by comparing the run rate of MCNP4A as a function of ENUM for a given cell size. Figure 1 compares the normalized run rate as a function of ENUM for four different voxel sizes. As ENUM is decreased from unity (analog simulation) to zero, the run rate increases in a linear fashion, an expected result since the code is tracking fewer particles. By normalizing the data for each voxel size to ENUM=1, the slope of each curve can be compared. For a $10 \times 10 \times 10$ mm^3 voxel the maximum run-rate difference is 29.6%, as compared to 9.7% for a voxel size of $3 \times 3 \times 3$ mm^3. This comparison suggests that as the voxel size is
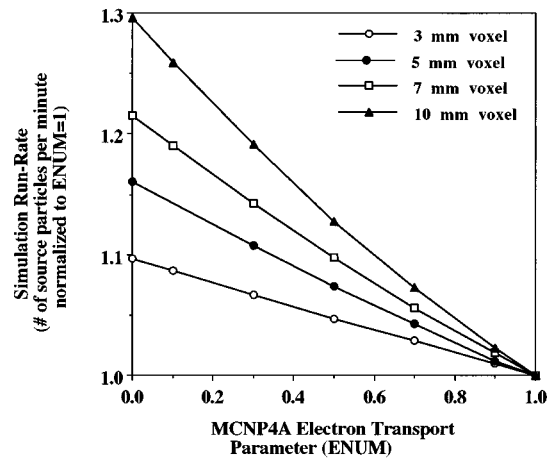

FIG. 1. Simulation run-rate for a 6 MV point source as a function of the MCNP4A secondary electron production parameter, ENUM. All data values are normalized to ENUM=1.0.

decreased, the code spends more time tracking the position of primary photons as opposed to producing and tracking the position of secondary electrons and photons. The timing analysis described above is based upon particle transport only and does not include the overhead associated with scoring energy deposition from photons and electrons in each individual lattice element. The simulation run rate decreases by a factor of greater than 540 as the number of tally elements increases above 1×10^4.

B. Algorithm development for photon transport modifications

A generalized Monte Carlo algorithm for tracking neutral particles will calculate the distance to the nearest boundary and compare this value with the distance to next collision. If the minimum distance represents a collision, the appropriate subroutines are called to sample the collision type and all parameters relating to the post-collision energy and angle of the primary and secondary particles. If the minimum distance represents the nearest boundary, the code updates the particle position from its present location into the new cell. The timing analysis demonstrates that although general, the algorithm in its present form is quite inefficient for the high resolution calculation matrices found in conventional radiotherapy treatment planning applications. The MCNP tracking subroutines account for the majority of time spent calculating the photon position for a typical radiotherapy simulation using lattice voxel sizes of 5 mm or less. This is to be expected, considering the average photon energy from a typical treatment linac. A typical 6 MV photon beam has an average photon energy of approximately 1.9 MeV, corresponding to a mean-free path in water of approximately 20 cm.

The MCNP4A package will support changes to the source code by utilizing the PRPR preprocessor and a patch file. This preprocessor is included as part of the standard MCNP4A distribution package. The UCLA photon tracking modifications utilize the standard MCNP4A lattice geometry as a framework for optimized transport, creating a patch file that
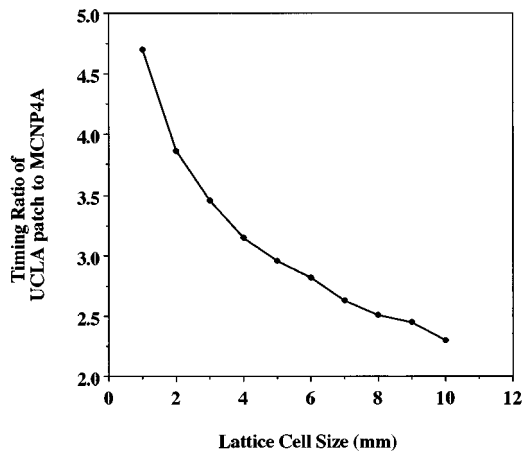
FIG. 2. The timing ratio between the UCLA tracking algorithm and the general MCNP4A algorithms for one SUN SPARC2 processor as a function of the lattice cell size. The source is based upon a 6 MV point source centered within a $30 \times 30 \times 30$ cm^3 water phantom.
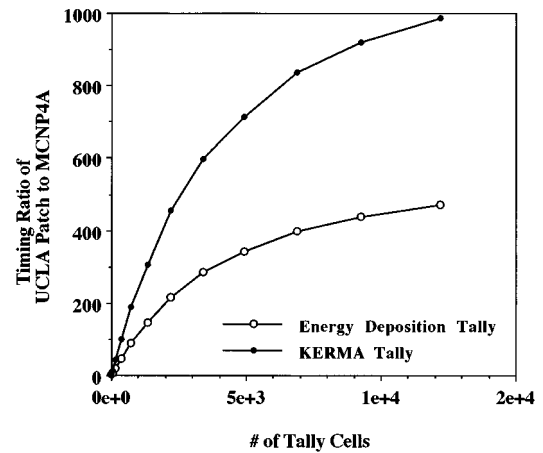

FIG. 3. The timing ratio between the UCLA tallying algorithm and the general MCNP4A algorithm for one SUN SPARC2 processor as a function of the number of tally elements. The source is based upon a 6 MV point source centered within a $30 \times 30 \times 30$ cm^3 water phantom and a $5 \times 5 \times 5$ mm^3 voxel size.

replaces the generalized MCNP tracking routines with an algorithm designed specifically for photon transport within the lattice geometry. While a particle is in the lattice phantom the algorithm calculates the minimum distance from the six bounding surfaces of the mesh cell. If the particle must cross one of the six surfaces the algorithm calculates the correct surface and increments the mesh location. Figure 2 illustrates the comparison between the UCLA tracking algorithm and the general MCNP4A algorithm. The simulation is based upon the 6 MV point source centered within a 30 $\times 30 \times 30$ cm^3 lattice water phantom. For a voxel size of 5 mm, the UCLA patch provides a performance increase of greater than three compared to the original MCNP4A simulation. As voxel size is decreased to 1 mm, the ratio of the UCLA time to the MCNP4A time increases to a factor of approximately 4.7.

C. Algorithm development for photon and electron dose tallies

MCNP4A supplies the user with two generalized tally algorithms for scoring dose deposition; pulse height and kerma. The pulse height tally scores the energy (MeV) of a photon or electron as it enters or leaves a lattice cell. A positive energy tally occurs from particles entering the lattice cell and a negative energy tally occurs when particles exit a lattice cell. The kerma tally scores absorbed dose (MeV/g) based upon the photon energy fluence and the mass energy absorption coefficient. The standard MCNP4A pulse height and kerma scoring algorithms currently check every lattice cell, regardless of whether the photon or electron has entered the cell. This is inefficient and poses a problem for dosimetry applications that require dose scoring for large 2-D or 3-D datasets. The UCLA patch replaces the standard pulse height and kerma scoring algorithms with a lattice specific algorithm. The energy deposition is only scored if a photon or electron enters a lattice cell designated as a tally cell. The standard pulse height tally is further modified to calculate the

dose (MeV/g) for a homogeneous or heterogeneous lattice. Figure 3 illustrates the comparison between the UCLA scoring algorithms and the general MCNP4A algorithms. The number of tally cells range from one at the center of the phantom to 12 167, based upon a $23 \times 23 \times 23$ tally cube. The UCLA patch produces a performance increase of greater than 470 for the standard pulse height tally as the number of tally elements increases above 1×10^4. For all data points tested the kerma tally is approximately two times faster than the pulse height tally. This occurs because the kerma algorithm is only called once when the particle crosses a lattice cell without a collision. The pulse height algorithm is called twice if the particle enters and exits the cell.

IV. RADIOTHERAPY SIMULATION RESULTS

A. Radiotherapy source library

In order to utilize MCNP4A bremsstrahlung calculations for radiation therapy, the target bremsstrahlung spectrum and resultant depth dose distribution from a Philips SL-15/25 linear accelerator has been modeled. Both machines are gantry mounted isocentric units (100 cm) providing two photon energies; 6 MV/25MV for the SL-25 and 6 MV/10MV for the SL-15. This work utilizes a two-step approach for simulating the depth dose characteristics from a linear accelerator. The first step requires a detailed simulation of the linac treatment head. This part of the simulation is calculated only once, since for a given energy, the geometry remains constant. The calculated bremsstrahlung spectra, differential in energy, angle, and position, are used in the second step to simulate the depth dose and profile characteristics of the machine.[23–25] Because the field size changes with each individual patient, this study simulates the movable jaws with the depth dose calculations, allowing for more exact simulation of the dose gradient along the beam edge and scattering effects from the collimator face. The mean energy of the electron beam incident on target is typically unknown and must be obtained by
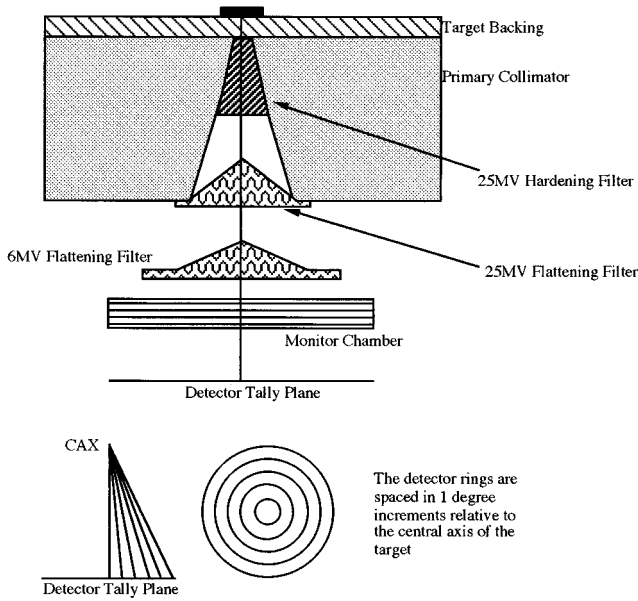
FIG. 4. MCNP4A simulation geometry for the linear accelerator treatment head. The detector tally plane is located is located 25 cm downstream from the front surface of the target. The circular rings correspond to the setup location for the MCNP4A ring detectors spaced in 1° increments relative to the beam central axis.
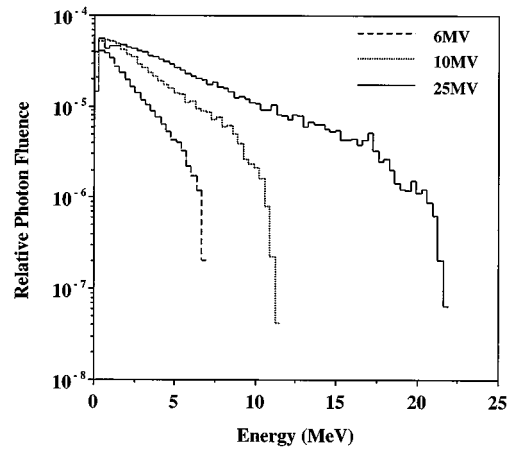

FIG. 5. The calculated bremsstrahlung spectra for the Philips 6, 10 and 25 MV photon beam energies. The next-event-estimator tally is located 25 cm downstream from the front surface of the target along the beam central axis. The three beam energies correspond to a mean electron energy on target of 6.8, 10.4, and 22.0 MeV for the 6, 10, and 25 MV photon beams, respectively.

calibrating each spectral distribution against the corresponding depth dose curve, and beam profile. A typical source calibration will employ a trial-and-error method by choosing a suitable mean electron energy exiting the flight tube. This method is also used by Rogers et al.[26] for calculating electron fluence spectra and Lovelock et al.[27] for simulating photon fluence spectra. The energy distribution of the electron beam exiting the vacuum line is assumed to have a Gaussian distribution with a standard deviation of approximately 3%, based upon the SL-25 technical documentation and conversations with the Philips engineers. After the initial electron energy is chosen, the bremsstrahlung phase space is scored at a point 25 cm downstream from the target. This consists of tallying the energy, angular, and spatial distribution of the bremsstrahlung spectra between the monitor chamber and the upper surface of the multileaf collimator. The MCNP4A next-event estimator (ring or point detector) is used to tally the bremsstrahlung energy distribution. Each ring is positioned as a function of the subtended angle from the target in 1° increments (see Fig. 4). This produces a simulated detector array that calculates the photon fluence, differential in energy and position. We have previously compared MCNP4A thick target bremsstrahlung calculations[28] versus the measurements of Faddegon et al.[29] for 15 MeV monoenergetic electrons incident on targets of Be, Al, and Pb. This analysis shows that MCNP4A is capable of calculating the integrated bremsstrahlung yield within 6% of measurement for angles less than 60°. Furthermore, the calculated mean energy is within 7% of the values derived from measurement for all angles tested. Figure 5 illustrates the 0°, central-axis bremsstrahlung spectra for the Philips 6, 10, and 25 MV beam energies.

In order to increase the efficiency of an actual treatment planning simulation the bremsstrahlung source calculations must be redefined as a generalized source model, preferably as a point or surface source approximation. The point source approximation is frequently used for Monte Carlo and convolution depth dose and profile calculations.[24,25,27,30] For the purposes of benchmark calculations and treatment planning simulations, the radiotherapy source is modeled as a modified point source whose location is defined by the virtual SSD of the Philips machines[31] and a Gaussian distribution (FWHM=1.5 mm)[32,33] in the x and y dimensions. In addition to position, the MCNP4A point source allows the user to sample for energy and polar angle. The angular distribution is sampled as the cosine of the polar angle (μ) with an intensity weighting based upon the integrated photon fluence for each radial tally ring.

B. Homogeneous phantom benchmarks

The RTMCNP SL-15 and SL-25 source library was benchmarked against standard depth dose and profile measurements. Figure 6 illustrates the comparison between MCNP4A depth dose calculations and water phantom measurements for the 6, 10, and 25 MV photon beams from the Philips SL15 and SL25 linear accelerator. The measurements were performed using a PTW water phantom and a 0.125 cm^3 PTW ion chamber (Model# N233642), with a machine SSD equal to 100 cm at the surface of the water phantom. Three field sizes were tested; 5×5 cm^2, 10×10 cm^2, and 15×15 cm^2. The depth dose calculations utilize a cylindrical tally cell with a grid spacing of 2 mm along the beam central axis and a cylinder radius based upon one-tenth the size of the open field. This produces a tally radius of 5, 10, and 15 mm for the 5×5, 10×10, and 15×15 cm^2 field sizes, respectively. The photon and electron low-energy cutoff was 10 and 500 keV, respectively, for the Monte Carlo calculation. The mean electron energy on target is 6.8,
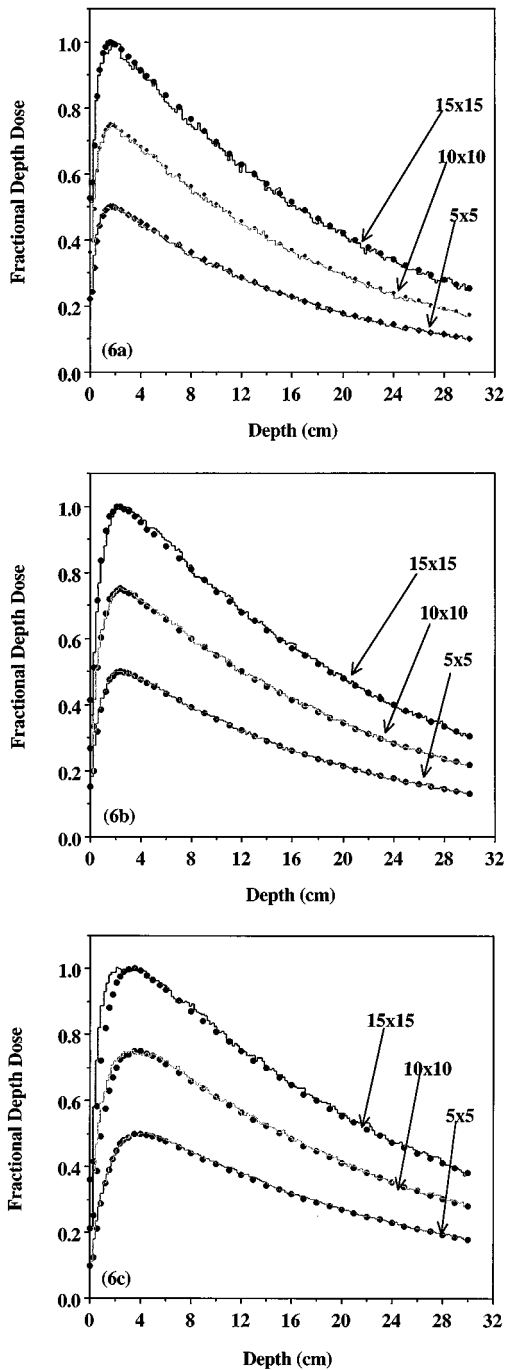
FIG. 6. The comparison of MCNP4A depth dose calculations versus water phantom measurements for the 6 MV (6a), 10 MV (6b), and 25 MV (6c) Philips SL-15/25 photon beams. The 5×5 and 10×10 cm^2 field size data have been scaled for inclusion on the same graph with all curves normalized to d_{max}. The MCNP4A calculations have a 1σ uncertainty of less than 2% for all data points tested. Electron contamination effects have been included for the 10×10 and 15×15 cm^2, 25 MV photon beam comparisons.
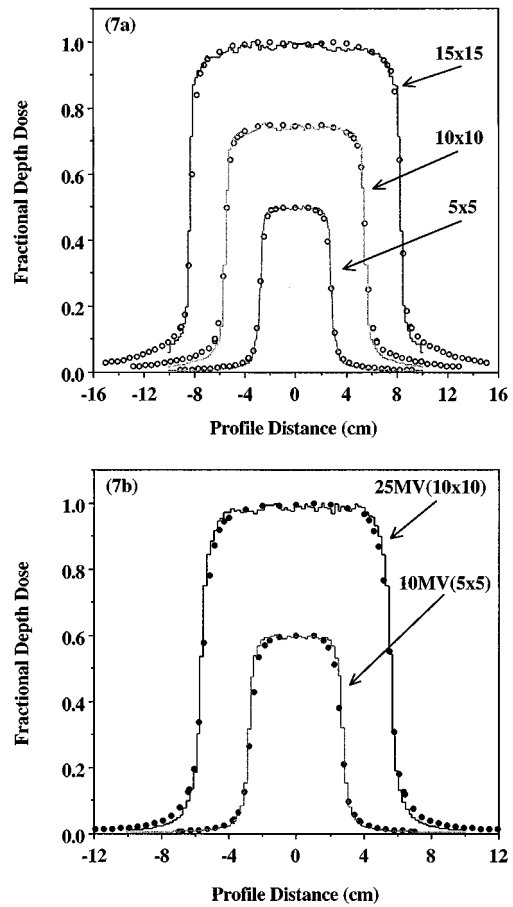

FIG. 7. The comparison of the MCNP4A profile calculations versus water phantom measurements for the 6 MV (7a), 10 MV, and 25 MV (7b) Philips SL-15/25 photon beams. The 5×5 and 10×10 cm^2 field size data have been scaled for inclusion on the same graph, with all curves normalized to the beam central axis. The MCNP4A calculations have a 1σ uncertainty of less than 2% for all data points tested.

10.4, and 22.0 MeV for the 6, 10, and 25 MV photon beams, respectively. This variable represents the final calibration energy for the bremsstrahlung spectral calculation. There is good agreement for the MCNP4A calculations versus measurement in all parts of the depth dose curve, including the buildup region. For the three beam energies at depths greater than or equal to d_{max}, the average ratio of the MCNP4A calculation to ion chamber measurement is 0.995 ± 0.012, 0.994 ± 0.015, and 0.993 ± 0.018 for the 5×5, 10×10, and 15×5 cm^2 field size, respectively. The 25 MV, 10×10 cm^2, and 15×15 cm^2 field size calculations represent a composite dose distribution of primary source photons and contamination electrons. The electron depth dose simulation is based upon a surface contamination source at the same position as the bremsstrahlung ring detector setup. The resultant electron depth dose curve is scaled according to the relative numbers of photons and electrons crossing the ring detector tally plane and added to the photon depth dose curve. The largest discrepancies between calculation and measurement occur in the buildup region for the 10×10 and 15×15 cm^2, 25 MV photon beam comparisons. This is mainly due to approximations associated with the contaminant electron source distribution and the scaling procedure.

Figure 7 illustrates the comparison between MCNP4A profile calculations and water phantom measurements for the three photon beam energies. The measurement and simulation setup is identical to the depth dose comparison, except for the profile tally plane. The profile measurements were

taken through the A–B plane (cross-table) at a depth of 10 cm in the water phantom. The MCNP4A simulations are based upon the same orientation, with 2 mm tally cell spacing along the profile axis. In general, MCNP agrees to within 3% of measured profile values within the 50%–100% isodose range. In the penumbra tail region (10%–20% isodose level) MCNP underestimates the dose profile by as much as 15%. The point source sampling model does not adequately account for the extrafocal source component from the actual treatment head, creating a narrower penumbral width, a result that is consistent with the deterministic model of Sharpe *et al.*[34] This limitation can be addressed by moving away from the point source model toward a complete phase-space source distribution at the exit of the monitor chamber.[26,35]

C. Heterogeneous phantom benchmarks

A high-density and low-density heterogeneity phantom was used to compare MCNP4A calculations with measurements. The high-density heterogeneity phantom of Masterson *et al.*[36] consists of a $3 \times 3 \times 10$ cm^3 cortical bone insert inserted into a $25 \times 25 \times 25$ cm^3 polystyrene support base with 28 TLD-100 rod inserts. The composition of the cortical bone insert is based upon the SB5 formulation of White[37] with a mass density of 1.87 g/cm^3. The low-density heterogeneity phantom is based upon a standard water-lung–water slab design consisting of 13 cm of dry water, 7.5 cm of low-density foam, and 15 cm of dry water with a cross-sectional area of 30×30 cm^2. The dry water is manufactured by Radiology Support Devices, Inc. and has a mass density of approximately 0.975 g/cm^3. A 7 mm cylindrical insert is machined in one dry water slab for acceptance of a standard PTW ion chamber. The low-density foam slabs are manufactured by the Dow Chemical Company and have a mass density of approximately 0.035 g/cm^3. Each individual foam slab has an approximate thickness of 1.88 cm based upon standard block cutting foam for electron blocks. A 7 mm cylindrical insert is machined along the central thickness of one foam slab for acceptance of a standard PTW ion chamber.

The measurement setup for the high-density heterogeneity is based upon a field size of 10×10 cm^2 and a SSD of 95 cm to the top of the phantom, with the beam central-axis symmetric through the bone heterogeneity. This places the machine isocenter at the center of the bone insert (TLD position #18). This location was chosen as the normalization point in order to match an exact TLD location and remain close to d_{max} on the descending portion of the depth dose curve. The central-axis depth dose measurements utilize TLD positions #13–#24. Film densitometry was also performed by positioning an X-OmatV readypack symmetrically through the center of the phantom. The MCNP4A simulation setup was identical to the measurement setup including the geometry, material, and position of the 12 LiF TLD rods. The low-energy photon and electron cutoffs were set to 10 and 500 keV, respectively, for particle transport throughout the simulation geometry. Figure 8 provides a benchmark comparison between the TLD measurements, film dosimetry, MCNP4A
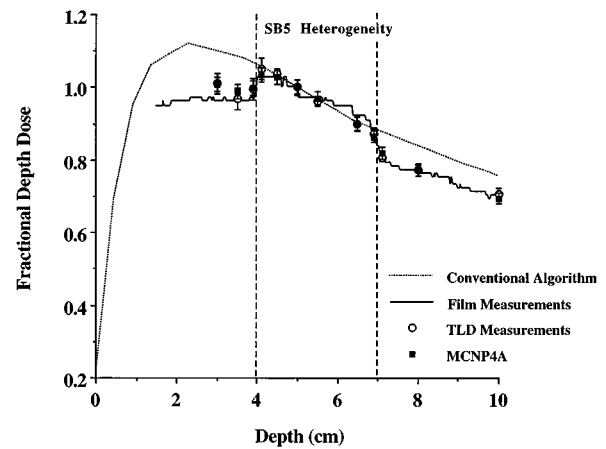

FIG. 8. High-density benchmark comparison between TLD measurements, film measurements, and the MCNP4A simulation and conventional treatment planning calculations for the 10 MV photon beam. The field size is 10×10 cm^2 with a SSD of 95.0 cm to the top of the phantom. All data sets are normalized to a depth of 5.0 cm.

calculations, and a conventional treatment planner for the 10 MV photon beam. The measurement and calculation comparisons were also performed for the 6 and 25 MV photon beams. The conventional algorithm calculates the photon dose to a point in a phantom by summing the primary and scattered dose components based upon empirical fits to measured water phantom data. The Wong–Henkelman correction factor is used to account for bulk heterogeneities[38] and the equivalent tissue–air-ratio (ETAR) method of Sontag and Cunningham is used for CT-based correction factors.[39] There is good agreement between the MCNP4A calculations and measurements for the three beam energies. The error bars (one standard deviation) for the calculations and the measurements overlap for the majority of data points. At shallower depths the film dosimetry underestimates the dose compared to MCNP4A. This is probably due to phantom design limitations using the readypack film, creating an air gap at the phantom entrance. The agreement of the conventional algorithm with film measurement and the MCNP4A calculation reveals a similar trend for all three energies. Within the bone heterogeneity there is good agreement due to the normalization point, but for depths beyond the heterogeneity the conventional algorithm consistently overestimates the depth dose. At a depth of 10 cm from the surface of the phantom, the conventional system calculates a depth dose that is 5.6%, 8.9%, and 17.6% greater than MCNP4A calculated values for the 6, 10, and 25 MV photon beams, respectively. The greater difference with increasing beam energy can be analyzed by examining the pair production cross section for the SB5 heterogeneity. Using the photon attenuation data of ICRU44 and the central-axis beam spectra for the three beam energies (Fig. 5) a fluence-weighted average for the pair production and total mass attenuation coefficient was computed. The fraction of photons attenuated within the SB5 material due to pair production events is 1.4%, 3.4%, and 8.0% for the 6, 10, and 25 MV photon beams, respectively. This relative increase with energy is in qualitative agreement with the
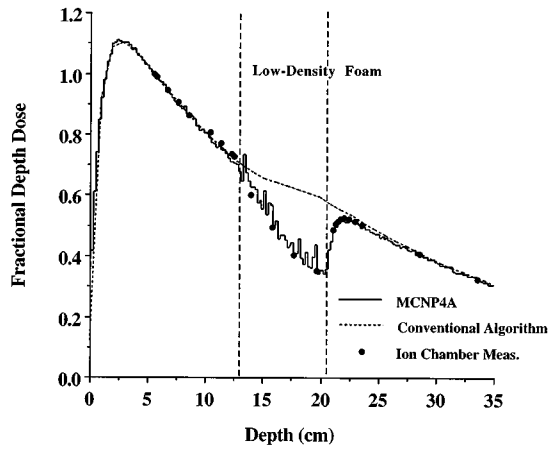
FIG. 9. Low-density benchmark comparison between ion chamber measurements and the MCNP4A and conventional treatment planning calculations for the 10 MV photon beam. The field size is 5×5 cm^2 with a SSD of 100.0 cm to the top of the phantom. All datasets are normalized to d_{max}.
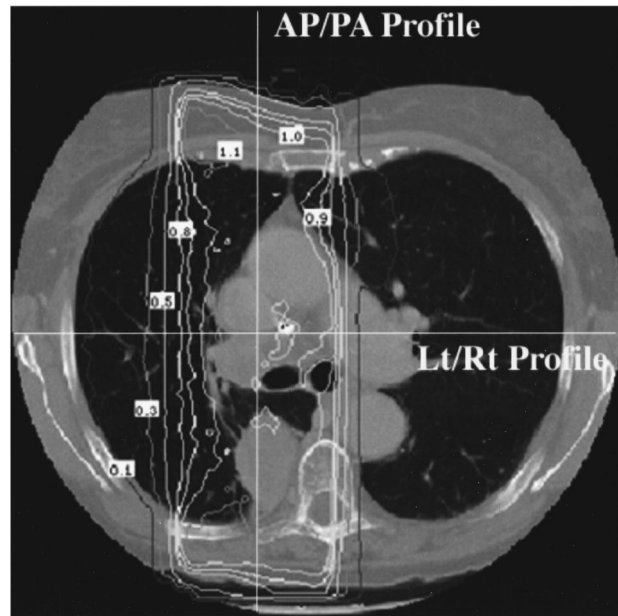

FIG. 10. The RTMCNP calculated dose distribution through the central-axis slice for a typical lung boost treatment plan using a beam energy of 10 MV and a field size of 8×8 cm^2. The simulation is normalized to the isocenter.

Monte Carlo comparisons given above. The ETAR correction is based upon electron density values derived from the original CT scan and therefore only accounts for changes in the incoherent scattering cross sections between polystyrene and SB5. It should be noted that this comparison applies only to the physics of photon and electron transport within the idealized geometry of the high-density heterogeneous phantom. There are very few locations within the human body with the consistent thickness and composition of cortical bone.

The measurement setup for the low-density heterogeneity is based upon a SSD of 100 cm to the top of the phantom with the beam central axis symmetric through the phantom and a field size of 5×5 cm^2. The measurements were taken with a PTW-0.125 cm^3 ion chamber (N233642) and a Keithley 35614E electrometer. The MCNP4A simulation setup modeled the solid water and low-density foam as closely as possible based upon the approximate elemental composition and mass density supplied by the manufacturer. The low-energy photon and electron cutoffs were set to 10 and 300 keV for photons and electrons, respectively, within the phantom. All measurements and calculations were normalized to a depth of approximately 5.5 cm corresponding to the first measured data point. Figure 9 provides a benchmark comparison between the UCLA ion chamber measurements, MCNP4A calculations, and the conventional algorithm for the 10 MV photon beam. There is good agreement with respect to the ion chamber measurements and MCNP4A calculations. For points within the foam slab there is a sharp dropoff in the depth dose curve due to the loss of lateral electronic equilibrium. The depth dose curve exhibits a small buildup region upon entering the downstream solid water section as electronic equilibrium is reestablished. The effect of statistical uncertainty is apparent for Monte Carlo calculated points within the foam slab. This is expected, given the lower photon interaction cross section for the foam heterogeneity versus the solid water phantom. The depth dose characteristics described above are consistent with the original analysis of

Mackie et al.,[40] who showed the influence of lateral electron scatter as a function of field size and beam energy. Solberg et al.[41] extended and verified this analysis by studying the secondary buildup region following an air gap as a function of small circular fields used for stereotactic radiosurgery. The conventional algorithm consistently overestimates the dose within the foam slab and secondary buildup region. This is to be expected since the Wong–Henkelman and ETAR heterogeneity correction methods do not account for secondary electron transport effects. The conventional calculations are in good agreement with the Monte Carlo calculations and measurements for points beyond the secondary buildup region, indicating the correct treatment of photon attenuation through the low-density slab.

D. Mediastinum treatment planning comparison

The mediastinum treatment planning analysis represents a qualitative comparison of the Monte Carlo method versus a conventional treatment planning algorithm. The setup is based upon a standard AP/PA two-field setup with the tumor located along the posterior wall of the right lung. The patient is positioned in the supine position and irradiated isocentrically with an anterior–posterior field (AP) and posterior–anterior field (PA) using a beam energy of 10 MV and a field size of 8×8 cm^2. The RTMCNP simulation was setup using 27 slices of the original CT scan, a slice spacing of 5 mm, and a calculation matrix of 64×64. This produces an $x-z$ voxel size of 4.4×4.4 mm^2 in the axial plane and a 5.0 mm y-voxel size based upon the slice thickness from the original CT scan. The isocenter location is identical for the conventional planner and RTMCNP and represents the normalization point for both calculation schemes. Figure 10 illustrates the axial dose distribution through the central slice for the
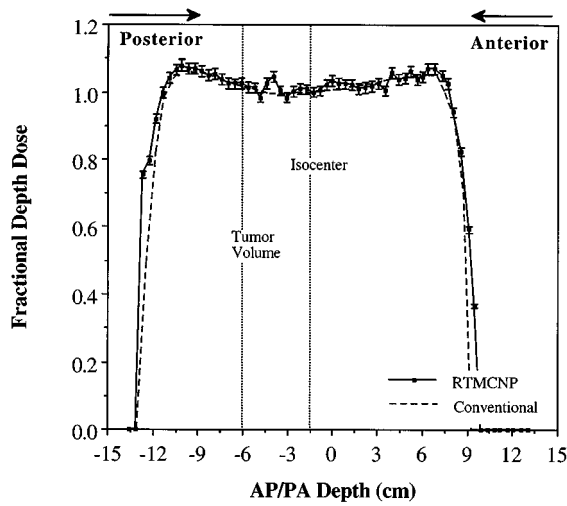
FIG. 11. A comparison of the AP/PA dose profile for the lung boost treatment plan calculated with RTMCNP and the conventional treatment planner. The profile is taken through the isocenter (see Fig. 10).

RTMCNP calculations. Figures 11 and 12 compare the central-axis dose distribution through the isocenter for the AP/PA field and RIGHT/LEFT profile, respectively. The AP/PA central-axis comparison shows good agreement, except within the buildup region. The conventional calculations are based upon empirical fits to measured data and the fitting procedure does not accurately model the dose distribution between the surface and the maximum dose point. The profile comparison illustrates the largest difference between RTMCNP and the conventional system and clearly shows the effect of lateral electron spreading into the right lung. RTMCNP predicts a smaller dose between the isocenter and the right field border and a larger dose between the right field border and the right chest wall. The conventional system overestimates the dose by up to 23% between the isocenter and the right field border 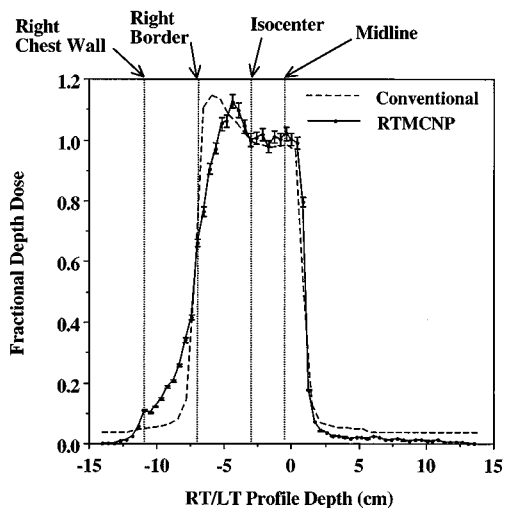and underestimates the dose by a factor of greater than 2 within the right lung. The underdose within the field border and overdose within the lung has implications for tumor control and normal tissue complications, respectively. Perez et al.[42] evaluated the results of a Radiation Therapy Oncology Group (RTOG 73-01) study regarding tumor control and overall survival for lung cancer patients treated with radiation. A total dose of 6000 cGy versus 4000–5000 cGy resulted in a higher complete response rate, intrathoracic tumor control, and three year survival. Marks presented a comprehensive overview of the pulmonary effects of thoracic irradiation.[43] The overall conclusion states that the total radiation dose as well as the volume of lung irradiated represent the two most important factors for predicting short-term and long-term lung injury. Implicit in these studies is the ability to accurately calculate the three-dimensional dose distribution within the lung; an area where Monte Carlo methods can provide a significant improvement over existing methods.

V. CONCLUSION

This study indicates that MCNP4A is a suitable candidate for photon-based radiotherapy calculations due to its specialized lattice geometry package and versatile source structure. The code package is maintained and modified by the Monte Carlo Transport Group at Los Alamos National Laboratory and is distributed through the Radiation Shielding and Information Center (RSIC). The RTMCNP graphical user interface developed at UCLA currently allows the user to automatically set up MCNP4A input files using the lattice geometry, an option that allows for homogeneous or heterogeneous dose calculations within individual voxel elements. The performance analysis indicates the code spends the majority of time tracking the position of source photons through the lattice geometry as well as tallying the energy deposition for individual lattice elements. Patch modifications to the transport subroutines have produced a run rate difference of approximately 4.7 using a voxel size of 1 mm^3. The tally modifications produce run-rate gains of approximately 470 based upon a tally section of greater than 1×10^4 lattice elements and a voxel size of 5 mm^3. The patch file developed for this work is easily integrated into the standard MCNP4A executable and is available to any interested user. There is satisfactory agreement between MCNP4A and measured data for a variety of homogeneous and heterogeneous benchmark comparisons. The mediastinum treatment planning comparison emphasizes the need for a complete dosimetry system that will account for all aspects of coupled photon–electron transport within heterogeneous media. This system is not intended to replace conventional treatment planning systems but can serve as an analysis tool for retrospective clinical comparisons and conventional algorithm development. Future work will concentrate on performance modifications, benchmarks, clinical comparisons, and the development of a PC-based multiprocessor computing platform.

FIG. 12. A comparison of the lateral dose profile for the lung boost treatment plan calculated with RTMCNP and the conventional treatment planner. The profile is taken through the isocenter (see Fig. 10).

ACKNOWLEDGMENTS

[a]Electronic mail: demarco@radonc.ucla.edu

[1]T. R. Mackie, P. Reckwerdt, and N. Papanikolaou, ''3-D photon beam dose algorithms,'' in *3-D Radiation Treatment Planning and Conformal Therapy*, edited by J. A. Purdy and B. Emami (Medical Physics Publishing Corporation, Madison WI, 1995).

[2]T. R. Mackie, P. Reckwerdt, T. McNutt, M. Gehring, and C. Sanders, ''Photon beam dose computations,'' in *Teletherapy: Present and Future*, edited by T. R. Mackie and J. R. Palta (Advanced Medical Publishing, Madison WI, 1996).

[3]Photon Treatment Planning Collaborative Working Group, ''Evaluation of high energy photon external beam treatment planning: Project summary,'' Int. J. Radiat. Oncol., Biol., Phys. **21**, 3 (1991).

[4]T. R. Mackie, S. S. Kubsad, D. W. O. Rogers, and A. F. Bielajew, ''The OMEGA project: Electron dose planning using Monte Carlo simulation,'' Med. Phys. **17**, 730 (1990) (abstract).

[5]D. W. O. Rogers, A. F. Bielajew, T. R. Mackie, and S. S. Kubsad, ''The OMEGA Project: Treatment planning for electron-beam radiotherapy using Monte Carlo techniques,'' Phys. Med. Biol. **35**, 285 (1990) (abstract).

[6]C. L. Hartmann-Siantar, W. P. Chandler, J. A. Rathkopf, M. M. Svatos, and R. M. White, ''PEREGRINE: An all-particle Monte Carlo code for radiation therapy,'' *Proceedings of the International Conference on Mathematics and Computations, Reactor Physics, and Environmental Analyses*, (American Nuclear Society, LaGrange Park, 1995), pp. 857–865.

[7]C. L. Hartmann-Siantar, W. P. Chandler, M. B. Chadwick, H. M. Blann, L. J. Cox, D. A. Resler, J. A. Rathkopf, T. R. Mackie, J. V. Siebers, M. A. Ross, P. M. DeLuca, Jr., K. A. Weaver, and R. M. White, ''Dose distributions calculated with the PEREGRINE all-particle Monte Carlo code,'' Med. Phys. **22**, 994 (1995).

[8]C. L. Hartmann-Siantar, W. P. Chandler, K. A. Weaver, N. W. Albright, L. J. Verhey, S. M. Hornstein, L. J. Cox, J. A. Rathkopf, and M. M. Svatos, ''Validation and performance assessment of the Peregrine all-particle Monte Carlo code for photon beam therapy,'' Med. Phys. **23**, 1128 (1996).

[9]L. E. Reinstein, E. B. Ramsay, J. Gajewski, S. Ramamoorthy, and A. G. Meek, ''SBNCT PLAN: a 3-dimensional treatment planning system for boron neutron capture therapy,'' in *Advances in Neutron Capture Therapy*, edited by A. H. Soloway *et al.* (Plenum, New York, 1993), pp. 171–175.

[10]R. G. Zamenhof, E. Redmond, G. Solares, D. Katz, K. Riley, and O. K. Harling, ''Monte Carlo-based treatment planning for boron neutron capture therapy using custom designed models automatically generated from CT data,'' Int. J. Radiat. Oncol., Biol., Phys. **35**, 383–397 (1996).

[11]J. F. Briesmeister, ''MCNP—A general Monte Carlo *N*-particle transport code, Version 4A,'' Los Alamos National Laboratory report, LA-12625, 1993.

[12]J. S. Hendricks and J. F. Briesmeister, ''Recent MCNP developments,'' Los Alamos National Laboratory report, LA-UR-91-3456, 1992.

[13]J. A. Halblieb and T. A. Mehlhorn ''ITS: The Integrated TIGER Series of coupled electron/photon Monte Carlo transport codes,'' Sandia National Laboratory report, SAND 84-0573, 1984.

[14]M. J. Berger and S. M. Seltzer, ''ETRAN, Monte Carlo code system for electron and photon transport through extended media,'' RSIC computer code package CCC-107, Oak Ridge National Laboratory Oak Ridge, TN, 1973.

[15]D. W. O. Rogers and A. F. Bielajew, ''Differences in electron depth-dose curves calculated with EGS and ETRAN and improved energy-range relationships,'' Med. Phys. **13**, 687–694 (1986).

[16]L. Landau, ''On the energy loss of fast particles by ionization,'' J. Phys. USSR **8**, 201 (1994).

[17]S. M. Seltzer, ''An overview of ETRAN Monte Carlo methods,'' in *The Monte Carlo Transport of Electrons and Photons*, edited by T. M. Jenkins, W. R. Nelson, and A. Rindi (Plenum, New York, 1988)

[18]R. J. Alfidi, W. J. MacIntyre, T. F. Meaney, E. S. Chernak, P. Janicki, R. Tarar, and H. Levin, ''Experimental studies to determine application of CAT scanning to the human body,'' Radiology **124**, 199 (1975).

[19]ICRP Publication 23, Report of the Task Group on Reference Man, 1975.

[20]ICRU Report 44, Tissue Substitutes in Radiation Dosimetry and Measurement, 1989.

[21]R. A. Brooks, L. G. Mitchell, C. M. O'Connor, and G. Di Chiro, ''On the relationship between computed tomography numbers and specific gravity,'' Phys. Med. Biol. **26**, 141–147 (1981).

[22]C. Constantinou, J. C. Harrington, and L. A. DeWerd, ''An electron density calibration phantom for CT-based treatment planning computers,'' Med. Phys. **19**, 325–327 (1992).

[23]P. L. Petti, M. S. Goodman, J. M. Sisterson, P. J. Biggs, T. A. Gabriel, and R. Mohan, ''Sources of electron contamination for the Clinac-35 25-MV photon beam,'' Med. Phys. **10**, 856–861 (1983).

[24]P. L. Petti, M. S. Goodman, T. A. Gabriel, and R. Mohan, ''Investigation of buildup dose from electron contamination of clinical photon beams,'' Med. Phys. **10**, 18–25 (1983).

[25]R. Mohan, C. Chui, and L. Lidofsky, ''Energy and angular distributions of photons from medical linear accelerators,'' Med. Phys. **12**, 592–597 (1985).

[26]D. W. O. Rogers, B. A. Faddegon, G. X. Ding, C. M. Ma, and J. We, ''BEAM: A Monte Carlo code to simulate radiotherapy treatment units,'' Med. Phys. **22**, 503–524 (1995).

[27]D. M. J. Lovelock, C. S. Chui, and R. Mohan, ''A Monte Carlo model of photon beams used in radiation therapy,'' Med. Phys. **22**, 1387–1394 (1995).

[28]J. J. DeMarco, T. D. Solberg, R. E. Wallace, and J. B. Smathers, ''A verification of the Monte Carlo code MCNP for thick target bremsstrahlung calculations,'' Med. Phys. **22**, 11–16 (1995).

[29]B. A. Faddegon, C. K. Ross, and D. W. O. Rogers, ''Angular distribution of bremsstrahlung from 15-MeV electrons incident on thick targets of Be, Al, and Pb,'' Med. Phys. **18**, 727–739 (1991).

[30]P. Metcalfe, T. Kron, A. Elliott, and T. Wong, ''Dosimetry of 6-MV x-ray beam penumbra,'' Med. Phys. **20**, 1439–1445 (1993).

[31]M. Tatcher and B. Bjarngard, ''Head-scatter factors and effective x-ray source positions in a 25-MV linear accelerator,'' Med. Phys. **19**, 685–686 (1992).

[32]D. A. Jaffray, J. J. Battista, A. Fenster, and P. Munro, ''X-ray sources of medical linear accelerators: Focal and extra-focal radiation,'' Med. Phys. **20**, 1417–1427 (1993).

[33]E. Loewenthal, E. Loewinger, E. Bar-Avraham, and G. Barnea, ''Measurement of the source size of a 6- and 18-MV radiotherapy linac,'' Med. Phys. **19**, 687–690 (1992).

[34]M. B. Sharpe, D. A. Jaffray, J. J. Battista, and P. Munro, ''Extrafocal radiation: A unified approach to the prediction of beam penumbra and output factors for megavoltage x-ray beams,'' Med. Phys. **22**, 2065–2074 (1995).

[35]C. L. Hartmann-Siantar, W. P. Chandler, K. A. Weaver, N. W. Albright, L. J. Verhey, S. M. Hornstein, L. J. Cox, J. A. Rathkopf, and M. M. Svatos, ''Validation and performance assessment of the Peregrine all-particle Monte Carlo code for photon beam therapy,'' Med. Phys. **23**, 1128 (1996).

[36]M. E. Masterson, G. Barest, C. Chui, K. P. Doppke, R. D. Epperson, W. B. Harms, K. E. Krippner, R. Mohan, E. D. Slessinger, M. R. Sontag, M. M. Urie, R. E. Wallace, and J. W. Wong, ''Interinstitutional experience in verification of external photon dose calculations,'' Int. J. Radiat. Oncol., Biol., Phys. **21**, 37–58 (1991).

[37]D. R. White, R. J. Martin, and R. Darlison, ''Epoxy resin based tissue substitutes,'' Br. J. Radiol. **50**, 814–821 (1977).

[38]M. J. Wong and R. M. Henkelman, ''A new approach to CT-pixel based photon dose calculations in heterogeneous media,'' Med. Phys. **10**, 199–208 (1983).

[39]M. R. Sontag and J. R. Cunningham, ''Corrections to absorbed dose calculations for tissue inhomogeneities,'' Med. Phys. **4**, 431–436 (1977).

[40]T. R. Mackie, E. El-Khatib, J. Battista, J. W. Scrimger, J. Van Dyk, and J. R. Cunningham, ''Lung dose corrections for 6- and 15-MV x rays,'' Med. Phys. **12**, 327 (1985).

[41]T. D. Solberg, F. E. Holly, A. A. F. DeSalles, R. E. Wallace, and J. B. Smathers, ''Implications of tissue heterogeneity for radiosurgery in head and neck tumors,'' Int. J. Radiat. Oncol. Biol. Phys. **32**, 235–239 (1995).

[42]C. A. Perez, M. Bauer, S. Edelstein, B. W. Gillespie, and R. Birch, ''Impact of tumor control on survival in carcinoma of the lung treated with irradiation,'' Int. J. Radiat. Oncol., Biol., Phys. **12**, 539–547 (1983).

[43]L. B. Marks, ''The pulmonary effects of thoracic irradiation,'' Oncology **8**, 89–100 (1994).